

Validating a bimodal intravascular ultrasound (IVUS) and near-infrared fluorescence (NIRF) catheter for atherosclerotic plaque detection in rabbits

Maxime Abran,^{1,2} Barbara E. Stähli,² Nolwenn Merlet,² Teodora Mihalache-Avram,² Mélanie Mecteau,² Eric Rhéaume,^{2,3} David Busseuil,² Jean-Claude Tardif,^{2,3} and Frédéric Lesage^{1,2,*}

¹Département de Génie Électrique and Institut de Génie Biomédical, École Polytechnique de Montréal, 2900 Édouard-Montpetit, Montreal, Qc, H3T 1J4, Canada

²Research Center, Montreal Heart Institute, 5000 Bélanger, Montreal, Qc, H1T 1C8, Canada

³Département de médecine, Université de Montréal, 2900 Édouard-Montpetit, Montreal, Qc, H3T 1J4, Canada
*frederic.lesage@polymtl.ca

Abstract: Coronary artery disease is characterized by atherosclerotic plaque formation. Despite impressive advances in intravascular imaging modalities, *in vivo* molecular plaque characterization remains challenging, and different multimodality imaging systems have been proposed. We validated an engineered bimodal intravascular ultrasound imaging (IVUS) / near-infrared fluorescence (NIRF) imaging catheter *in vivo* using a balloon injury atherosclerosis rabbit model. Rabbit aortas and right iliac arteries were scanned *in vivo* after indocyanine green (ICG) injection, and compared to corresponding *ex vivo* fluorescence and white light images. Areas of ICG accumulation were colocalized with macroscopic atherosclerotic plaque formation. *In vivo* imaging was performed with the bimodal catheter integrating ICG-induced fluorescence signals into cross-sectional IVUS imaging. *In vivo* ICG accumulation corresponded to *ex vivo* fluorescence signal intensity and IVUS identified plaques.

©2015 Optical Society of America

OCIS codes: (170.0110) Imaging systems; (110.7170) Ultrasound; (170.6280) Spectroscopy; fluorescence and luminescence; (170.2150) Endoscopic imaging.

References and links

1. M. D. Huffman, D. M. Lloyd-Jones, H. Ning, D. R. Labarthe, M. Guzman Castillo, M. O'Flaherty, E. S. Ford, and S. Capewell, "Quantifying options for reducing coronary heart disease mortality by 2020," *Circulation* **127**(25), 2477–2484 (2013).
2. P. Libby, "Inflammation in atherosclerosis," *Nature* **420**(6917), 868–874 (2002).
3. P. Libby, "Atherosclerosis: disease biology affecting the coronary vasculature," *Am. J. Cardiol.* **98**(12 12A), 3Q–9Q (2006).
4. P. Libby, "Inflammation in atherosclerosis," *Arterioscler. Thromb. Vasc. Biol.* **32**(9), 2045–2051 (2012).
5. J.-C. Tardif, J. Grégoire, P. L. L'Allier, R. Ibrahim, M.-A. Lavoie, M. LeMay, E. Cohen, S. Levesque, P.-F. Keller, T. Heinonen, and M.-C. Guertin, "Effect of atherosclerotic regression on total luminal size of coronary arteries as determined by intravascular ultrasound," *Am. J. Cardiol.* **98**(1), 23–27 (2006).
6. S.-J. Kang, G. S. Mintz, T. Akasaka, D.-W. Park, J.-Y. Lee, W.-J. Kim, S.-W. Lee, Y.-H. Kim, C. Whan Lee, S.-W. Park, and S.-J. Park, "Optical coherence tomographic analysis of in-stent neoatherosclerosis after drug-eluting stent implantation," *Circulation* **123**(25), 2954–2963 (2011).
7. S. Tahara, T. Morooka, Z. Wang, H. G. Bezerra, A. M. Rollins, D. I. Simon, and M. A. Costa, "Intravascular optical coherence tomography detection of atherosclerosis and inflammation in murine aorta," *Arterioscler. Thromb. Vasc. Biol.* **32**(5), 1150–1157 (2012).
8. S. E. Nissen and P. Yock, "Intravascular ultrasound: novel pathophysiological insights and current clinical applications," *Circulation* **103**(4), 604–616 (2001).

9. F. A. Jaffer, M. A. Calfon, A. Rosenthal, G. Mallas, R. N. Razansky, A. Mauskopf, R. Weissleder, P. Libby, and V. Ntziachristos, "Two-dimensional intravascular near-infrared fluorescence molecular imaging of inflammation in atherosclerosis and stent-induced vascular injury," *J. Am. Coll. Cardiol.* **57**(25), 2516–2526 (2011).
10. F. A. Jaffer, C. Vinegoni, M. C. John, E. Aikawa, H. K. Gold, A. V. Finn, V. Ntziachristos, P. Libby, and R. Weissleder, "Real-time catheter molecular sensing of inflammation in proteolytically active atherosclerosis," *Circulation* **118**(18), 1802–1809 (2008).
11. M. Nahrendorf, F. A. Jaffer, K. A. Kelly, D. E. Sosnovik, E. Aikawa, P. Libby, and R. Weissleder, "Noninvasive vascular cell adhesion molecule-1 imaging identifies inflammatory activation of cells in atherosclerosis," *Circulation* **114**(14), 1504–1511 (2006).
12. L. Rouleau, R. Berti, V. W. K. Ng, C. Matteau-Pelletier, T. Lam, P. Saboural, A. K. Kakkar, F. Lesage, E. Rhéaume, and J.-C. Tardif, "VCAM-1-targeting gold nanoshell probe for photoacoustic imaging of atherosclerotic plaque in mice," *Contrast Media Mol. Imaging* **8**(1), 27–39 (2013).
13. B. M. Wallis de Vries, J.-L. Hillebrands, G. M. van Dam, R. A. Tio, J. S. de Jong, R. H. J. A. Slart, and C. J. Zeebregts, "Images in cardiovascular medicine. Multispectral near-infrared fluorescence molecular imaging of matrix metalloproteinases in a human carotid plaque using a matrix-degrading metalloproteinase-sensitive activatable fluorescent probe," *Circulation* **119**(20), e534–e536 (2009).
14. C. Vinegoni, I. Botnaru, E. Aikawa, M. A. Calfon, Y. Iwamoto, E. J. Folco, V. Ntziachristos, R. Weissleder, P. Libby, and F. A. Jaffer, "Indocyanine Green Enables Near-Infrared Fluorescence Imaging of Lipid-Rich, Inflamed Atherosclerotic Plaques," *Sci. Transl. Med.* **3**(84), 84ra45 (2011).
15. J. Caesar, S. Shaldon, L. Chianidussi, L. Guevara, and S. Sherlock, "The use of indocyanine green in the measurement of hepatic blood flow and as a test of hepatic function," *Clin. Sci.* **21**, 43–57 (1961).
16. R. W. Flower and B. F. Hochheimer, "Indocyanine green dye fluorescence and infrared absorption choroidal angiography performed simultaneously with fluorescein angiography," *Johns Hopkins Med. J.* **138**(2), 33–42 (1976).
17. G. J. Ughi, J. Verjans, A. M. Fard, H. Wang, E. Osborn, T. Hara, A. Mauskopf, F. A. Jaffer, and G. J. Tearney, "Dual modality intravascular optical coherence tomography (OCT) and near-infrared fluorescence (NIRF) imaging: a fully automated algorithm for the distance-calibration of NIRF signal intensity for quantitative molecular imaging," *Int. J. Cardiovasc. Imaging* **31**, 259–268 (2014).
18. T. Desmettre, J. M. Devoisselle, and S. Mordon, "Fluorescence Properties and Metabolic Features of Indocyanine Green (ICG) as Related to Angiography," *Surv. Ophthalmol.* **45**(1), 15–27 (2000).
19. J.-C. Tardif, F. Lesage, F. Harel, P. Romeo, and J. Pressacco, "Imaging Biomarkers in Atherosclerosis Trials," *Circ Cardiovasc Imaging* **4**(3), 319–333 (2011).
20. D. N. Stephens, J. Park, Y. Sun, T. Papaioannou, and L. Marcu, "Intraluminal fluorescence spectroscopy catheter with ultrasound guidance," *J. Biomed. Opt.* **14**(3), 030505 (2009).
21. A. J. Dixon and J. A. Hossack, "Intravascular near-infrared fluorescence catheter with ultrasound guidance and blood attenuation correction," *J. Biomed. Opt.* **18**(5), 056009 (2013).
22. J. Bec, D. M. Ma, D. R. Yankelevich, J. Liu, W. T. Ferrier, J. Southard, and L. Marcu, "Multispectral fluorescence lifetime imaging system for intravascular diagnostics with ultrasound guidance: in vivo validation in swine arteries," *J. Biophotonics* **7**(5), 281–285 (2014).
23. M. Abran, G. Cloutier, M. H. Cardinal, B. Chayer, J.-C. Tardif, and F. Lesage, "Development of a photoacoustic, ultrasound and fluorescence imaging catheter for the study of atherosclerotic plaque," *IEEE Trans. Biomed. Circuits Syst.* **8**(5), 696–703 (2014).
24. D. T. Delpy, M. Cope, P. van der Zee, S. Arridge, S. Wray, and J. Wyatt, "Estimation of optical pathlength through tissue from direct time of flight measurement," *Phys. Med. Biol.* **33**(12), 1433–1442 (1988).
25. D. N. Ku, D. P. Giddens, C. K. Zarins, and S. Glagov, "Pulsatile flow and atherosclerosis in the human carotid bifurcation. Positive correlation between plaque location and low oscillating shear stress," *Arteriosclerosis* **5**(3), 293–302 (1985).
26. M. Naghavi, P. Libby, E. Falk, S. W. Casscells, S. Litovsky, J. Rumberger, J. J. Badimon, C. Stefanadis, P. Moreno, G. Pasterkamp, Z. Fayad, P. H. Stone, S. Waxman, P. Raggi, M. Madjid, A. Zarrabi, A. Burke, C. Yuan, P. J. Fitzgerald, D. S. Siscovick, C. L. de Korte, M. Aikawa, K. E. Airaksinen, G. Assmann, C. R. Becker, J. H. Chesebro, A. Farb, Z. S. Galis, C. Jackson, I. K. Jang, W. Koenig, R. A. Lodder, K. March, J. Demirovic, M. Navab, S. G. Priori, M. D. Reikhter, R. Bahr, S. M. Grundy, R. Mehran, A. Colombo, E. Boerwinkle, C. Ballantyne, W. Insull, Jr., R. S. Schwartz, R. Vogel, P. W. Serruys, G. K. Hansson, D. P. Faxon, S. Kaul, H. Drexler, P. Greenland, J. E. Muller, R. Virmani, P. M. Ridker, D. P. Zipes, P. K. Shah, and J. T. Willerson, "From vulnerable plaque to vulnerable patient: a call for new definitions and risk assessment strategies: Part II," *Circulation* **108**(15), 1772–1778 (2003).
27. N. D. Desai, S. Miwa, D. Kodama, G. Cohen, G. T. Christakis, B. S. Goldman, M. O. Baerlocher, M. P. Pelletier, and S. E. Fremes, "Improving the quality of coronary bypass surgery with intraoperative angiography: validation of a new technique," *J. Am. Coll. Cardiol.* **46**(8), 1521–1525 (2005).
28. S. Yoneya, T. Saito, Y. Komatsu, I. Koyama, K. Takahashi, and J. Duvoll-Young, "Binding properties of indocyanine green in human blood," *Invest. Ophthalmol. Vis. Sci.* **39**(7), 1286–1290 (1998).
29. S. Lee, M. W. Lee, H. S. Cho, J. W. Song, H. S. Nam, D. J. Oh, K. Park, W.-Y. Oh, H. Yoo, and J. W. Kim, "Fully integrated high-speed intravascular optical coherence tomography/near-infrared fluorescence structural/molecular imaging in vivo using a clinically available near-infrared fluorescence-emitting indocyanine

- green to detect inflamed lipid-rich atheromata in coronary-sized vessels,” *Circ. Cardiovasc. Interv.* **7**(4), 560–569 (2014).
30. H. Yoo, J. W. Kim, M. Shishkov, E. Namati, T. Morse, R. Shubochkin, J. R. McCarthy, V. Ntziachristos, B. E. Bouma, F. A. Jaffer, and G. J. Tearney, “Intra-arterial catheter for simultaneous microstructural and molecular imaging *in vivo*,” *Nat. Med.* **17**(12), 1680–1684 (2011).
31. D. Busseuil, Y. Shi, M. Mecteau, G. Brand, A.-E. Kernalguen, E. Thorin, J.-G. Latour, E. Rhéaume, and J.-C. Tardif, “Regression of aortic valve stenosis by ApoA-I mimetic peptide infusions in rabbits,” *Br. J. Pharmacol.* **154**(4), 765–773 (2008).
-

1. Introduction

Cardiovascular diseases are the leading cause of morbidity and mortality worldwide [1], and their burden is expected to rise in the near future given the aging of the population and the increasing rates of obesity and diabetes. Cardiovascular diseases are mainly due to atherosclerotic changes within the vessel wall [2], with lipoprotein accumulation and inflammatory cell proliferation considered as key factors in atherosclerotic plaque formation [3,4].

Despite impressive advances in non-invasive and invasive imaging approaches, the identification of high-risk coronary artery plaques prior to their rupture, and thereby identification of patients at risk for acute events, remains an unmet challenge. As vulnerable plaques are often not flow-limited, they remain undetected by conventional coronary angiography [3]. Different imaging modalities including intravascular ultrasound (IVUS) and optical coherence tomography (OCT) have been established to overcome these limitations [5–7]. Although such catheter-based technologies provide high-resolution cross-sectional images of the coronary artery wall, allowing for a detailed visualization of atherosclerotic plaques and corresponding vessel responses [8], information with regard to plaque composition and activity is limited. In recent years, emerging molecular imaging approaches such as near-infrared fluorescence (NIRF) imaging have been proposed for an improved plaque characterization at a cellular or molecular level. Utilizing a variety of molecular probes, fluorescence imaging has been demonstrated to provide complementary information with regard to plaque activity and inflammation [9–13]. Among others, indocyanine green (ICG), given its ability to accumulate in lipid-loaded macrophages [14] and its established clinical applications [15,16], has been proposed as an attractive agent for molecular fluorescence imaging of cardiovascular diseases [14,17]. ICG is a near-infrared fluorochrome known to bind to albumin, which is ingested by macrophages [18]. However, for *in vivo* imaging, sensitive molecular technologies need to be combined with high-resolution microstructural imaging tools to allow for a correct interpretation of the fluorescence signal. Advantages of integrated multimodality catheter designs and simultaneous imaging have been recognized [17,19]. Fluorescence imaging catheters with integrated ultrasound guidance have been designed previously [20,21] and validated *in vivo* in swine arteries [22]. However, previous *in vivo* applications relied on balloon occlusion to remove blood from the field of view.

In this study, we validated our recently engineered bimodal IVUS/NIRF imaging catheter without balloon occlusion *in vivo* using a rabbit model of atherosclerosis [23]. Further, *in vivo* fluorescence imaging was compared to *ex vivo* ICG accumulation and macroscopic plaque formation, and a blood attenuation compensation algorithm for fluorescence imaging was proposed.

2. Materials and methods

2.1 Animal model of atherosclerosis

Inflamed atheroma formation was induced in 9 male New Zealand White rabbits (2.8–3 kg, aged 12–13 weeks; Charles River Laboratories, Saint-Constant, QC, Canada) using a 14-week-cholesterol-enriched diet (0.5% cholesterol, Harlan Teklad Diets, Madison, WI; $n = 3$) or an artery balloon injury ($n = 3$), or both ($n = 3$). Balloon injury was performed in the abdominal aorta and the right iliac artery at week 2. At week 14, *in vivo* and *ex vivo* imaging

procedures were performed, and the animals were sacrificed thereafter by exsanguination under anesthesia.

The experimental protocol was approved by the animal ethics committee of the Montreal Heart Institute Research Center according to the guidelines of the Canadian Council on Animal Care.

2.2 Balloon dilation procedures

For balloon injury procedures, anesthesia was induced with intramuscular injections of ketamine (35 mg/kg) and buprenorphine (10 µg/kg), and maintained with inhaled isoflurane (3 to 5% v/v, Baxter, Deerfield, IL) and supplemental oxygen [10]. Then, a 5F transradial introducer (Cordis Corporation, Fremont, CA) was installed into the right carotid artery, and a 0.014" guidewire (Abbott Vascular, Santa Clara, CA) advanced to the aorta. Balloon injury was performed under fluoroscopic guidance utilizing a percutaneous transluminal coronary angiography (PTCA) balloon dilatation catheter (Boston Scientific, Marlborough, MA) inflated to tension. Balloon injury was performed in the proximal 20 mm of the right iliac artery (2.5-mm balloon), and in the distal 40 mm of the abdominal aorta above the iliac bifurcation (4-mm balloon). Three pullbacks were performed in each arterial segment. The left iliac artery served as non-injured controls. After balloon injury and removal of the introducer, the right carotid artery was ligated.

2.3 Bimodal intravascular ultrasound (IVUS) / near-infrared fluorescence (NIRF) catheter system

The imaging system consisting of an imaging catheter linked to an optical assembly and custom-made electronics, has previously been described and is shown in Fig. 1 [23]. It combined an 400 µm optical fiber having a numerical aperture of 0.22 for 2-dimensional, 360-degree fluorescence imaging and photoacoustic excitation, and an ultrasound transducer (extracted from a commercially available IVUS 45 MHz catheter; Revolution, Volcano Therapeutics, Rancho Cordova, CA), for acoustic imaging and photoacoustic signal detection at frame rates of up to 30 images/second. A 500 µm right angle prism with an aluminized hypotenuse was glued to the optical fiber for side-fire illumination. With a diameter of 1.4 mm, the system was utilized with 5F introducers. In this work, we focused exclusively on IVUS and NIRF.

A dedicated electronic circuit synchronized acquisition of the different imaging modalities with 2 motors driving the rotating/translating catheter assembly. The pullback speed was set to 0.5 mm/second, with a total pullback length of 100 mm and a frame rate of 10 images/second. A custom Matlab (The MathWorks, Inc, Natick, MA) user interface was used for USB data acquisition, real-time signal filtering, reconstruction, and image display. Optical and electrical connections between the fixed and rotating assemblies used an optical rotary joint for fluorescence imaging (Doric Lenses, Quebec, QC, Canada) and a slip ring to transmit and receive ultrasound signals. A 20 dB preamplifier was designed to rotate with the ultrasound transducer, in order to amplify the signal close to the source. The main ultrasound acquisition circuit included a 5 to 55 dB variable gain amplifier with customizable time-gain compensation and a 14-bit, 200 MegaSamples/second analog-to-digital converter.

Fluorescence excitation was performed with a 780 nm laser diode combined with a narrow-band optical filter (769 ± 20 nm) and emission was detected by a photomultiplier tube (H5783-20, Hamamatsu Photonics, Hamamatsu City, Japan) combined with a narrow-band optical filter (832 ± 19 nm). A dichroic filter (cut-off wavelength: 801 nm) was used to separate the excitation and emission light paths. The optical power at the tip of the catheter was 25 mW. In our phantom validations, we detected 100 nM of ICG through 1.4 mm of blood-mimicking solution. The lateral resolution through blood was 500 µm for an object at 1.3 mm of the outer surface of the catheter.

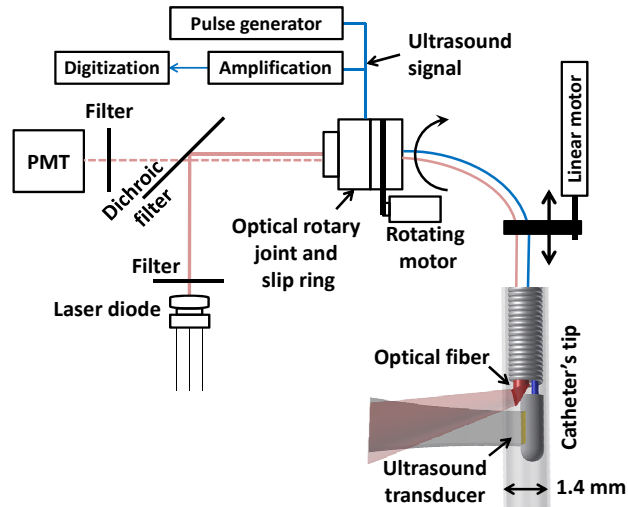


Fig. 1. Overview of the IVUS-NIRF imaging system with a diagram of the catheter's tip. PMT stands for photomultiplier tube and is the optical detector in NIRF.

2.4 *In vivo* intravascular imaging procedures

Imaging procedures were performed as previously described. Animals were anesthetised with intramuscular injections of ketamine (35 mg/kg) and buprenorphine (10 µg/kg), followed by isoflurane (3 to 5% v/v) inhalation. For intravascular imaging procedures, the fluorochrome ICG (10 mg/kg) was utilized, and injected via the right ear vein at the beginning of the procedures. While the fluorochrome was circulating, a 5F introducer was inserted into the left carotid artery, and the bimodal imaging catheter was advanced over the 0.014" guide wire under fluoroscopic guidance. The guide wire was removed prior to image acquisition. Forty minutes after ICG injection, automated imaging pullbacks were performed using the bimodal IVUS/NIRF imaging catheter both in the right iliac artery and the abdominal aorta.

2.5 Intravascular ultrasound (IVUS)/ near-infrared fluorescence (NIRF) image analysis

For the 100 mm pullback, manual segmentation of the vessel wall was performed on recorded IVUS images using 1 slice/mm, and interpolation was used to obtain the distance for the remaining slices in between (1900 slices). A dedicated fluorescence blood attenuation compensation algorithm based on the Beer-Lambert law [24] was developed to compensate the fluorescence signal amplitude for the calculated distance between the imaging catheter and the arterial wall. We observed compensation to be dependent on vessel size. Utilizing an effective extinction coefficient of 2 mm⁻¹ was found to be optimal for the vessel sizes that were imaged. For fluorescence detection, a minimum catheter-vessel wall distance of 0.1 mm based on the limitation of IVUS imaging, and a maximum distance of 0.75 mm to avoid background noise were utilized. The blood attenuation compensation algorithm was applied to all the results presented below, unless otherwise specified. Assuming fluorescence to be preferentially accumulated at the vessel lumen surface, an algorithm was applied on the NIRF data for each longitudinal position to account for light attenuation by blood in the lumen. Due to the expected homogeneity of the media, a simple Beer-Lambert law was assumed and is given by,

$$F_c(\theta) = F_m(\theta) e^{2\mu d(\theta)} \quad (1)$$

where F_c is the corrected fluorescence signal, F_m is the measured fluorescence signal at each angular position θ , μ is the extinction coefficient and d is the distance between the catheter and the vessel wall.

2.6 Ex vivo imaging

After the sacrifice, animals were perfused with Lactated Ringers solution. Aortas and iliac arteries were excised, conserved in 4% formaldehyde and imaged within 30 minutes in a fluorescence imaging scanner (IVIS Lumina II, Caliper Life Sciences, Hopkinton, MA). The abdominal aorta and iliac arteries of one randomly chosen rabbit per group were opened longitudinally, pinned on a black tray and imaged *en face*. White light images captured with a camera (D3100, Nikon Corporation, Tokyo, Japan) at an exposure time of 1/15 second for macroscopic atherosclerotic plaque visualization and fluorescence imaging utilizing the fluorescence scanner for *ex vivo* ICG accumulation detection were performed. For fluorescence, excitation and emission wavelengths were set to 745 nm and 800 nm, respectively. The exposure time was 1 second and no binning was applied.

3. Results

3.1 Ex vivo near-infrared fluorescence (NIRF) imaging: validation of the model

Ex vivo fluorescence imaging was performed for the entire aorta, as well as for the right balloon-injured and the left non-injured iliac arteries (Fig. 2). An increased NIRF signal in balloon-injured arterial segments was observed both for rabbits fed a regular diet and rabbits fed a cholesterol-enriched diet (3 per group; Fig. 2(a)-2(c) and 2(g)-2(i), respectively) as compared to non-injured arterial segments of rabbits fed a cholesterol-enriched diet (Fig. 2(d)-2(e)). The strongest NIRF signal was observed in balloon-injured arterial segments of rabbits fed a cholesterol-enriched diet (Fig. 2(g)-2(i)). The increased NIRF signal was quantified and is illustrated in Fig. 3, where the signal ratio between right and left iliac arteries and between distal 0-40 mm and 40-80 mm abdominal aorta is compared for each group.

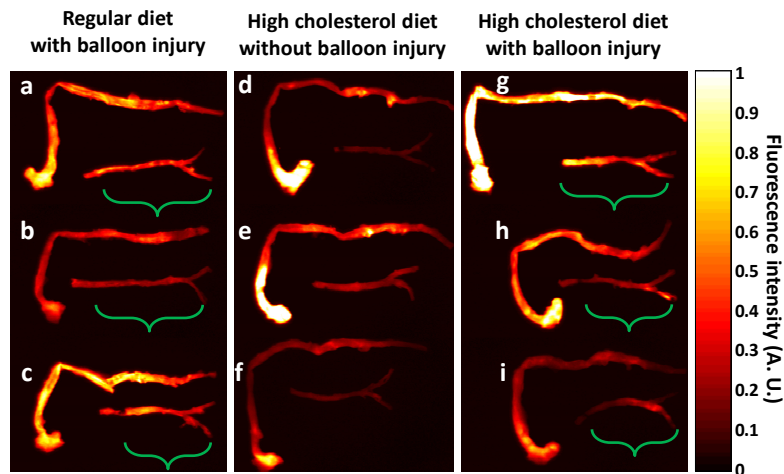


Fig. 2. *Ex vivo* near-infrared fluorescence (NIRF) images of rabbit aortas. Each column represents a different group, with 3 rabbits per group. Rabbit aortas were cut in two sections to fit in the field of view of the imaging system. For each panel, the upper part represents the aortic arch, the thoracic aorta and the proximal abdominal aorta. The lower part represents the continuation of the abdominal aorta and the left (top) and right (bottom) iliac arteries. Green brackets indicate areas of balloon injury. A.U., arbitrary units.

Substantial ICG accumulation was observed in the aortic arch and the descending thoracic aorta (Fig. 2(a)-2(i)), as both regions are prone to atherosclerotic plaque formation given the increased shear stress oscillation [25]. The ICG accumulation in these arterial segments was further enhanced in the cholesterol-enriched diet group.

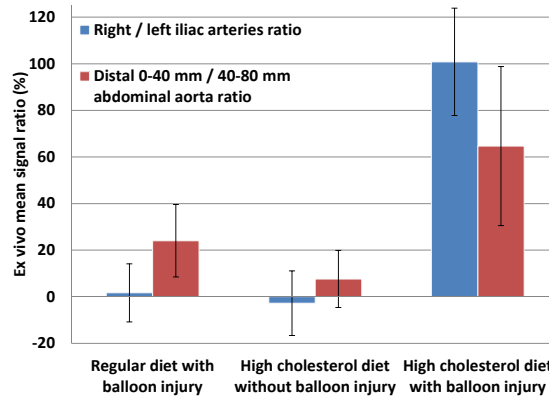


Fig. 3. Signal comparison for selected arterial segments in *ex vivo* near-infrared fluorescence (NIRF) images. The distal 0-40 mm abdominal aorta and the right iliac artery are the balloon-injured regions, when performed. The ratios were obtained by dividing the mean right iliac artery (or distal 0-40 mm abdominal aorta) signal by the mean left iliac artery (or distal 40-80 mm abdominal aorta) signal for each animal. The error bars are the standard errors on the mean for the three rabbits of each group.

En face fluorescence and white light imaging are shown in Fig. 4. In rabbits fed a cholesterol-enriched diet, ICG-induced signal enhancement on fluorescence imaging was colocalized with severely diseased atherosclerotic vessel regions as identified by their opaque and white macroscopic appearance on white light (Fig. 4(c)-4(f)). Similarly, at sites of balloon injury, increased ICG accumulation was observed at sites of scar tissue formation (Fig. 4(a)-4(b), and 4(e)-4(f)).

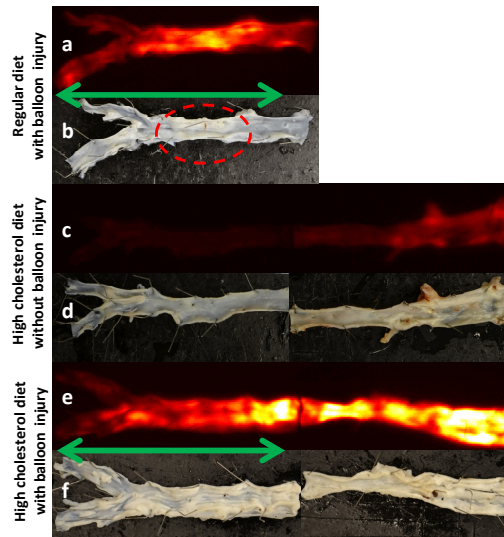


Fig. 4. Paired *ex vivo* near-infrared fluorescence (NIRF) and white light images of three longitudinally opened rabbit aortas, one for each group. (a, c, e) *Ex vivo* fluorescence images of excised aorta and iliac arteries showing increased ICG-accumulation in balloon-injured areas and in rabbits fed a cholesterol-enriched diet. (b, d, f) White light images of excised aorta and iliac arteries showing corresponding macroscopic plaque formation. The red circle shows scar tissue caused by the balloon injury. The green arrows show the regions that underwent balloon injury, including the right iliac artery (bottom).

3.2 *In vivo* intravascular ultrasound (IVUS) / near-infrared fluorescence (NIRF) imaging

The integration of fluorescence and IVUS imaging in a single catheter allows for simultaneous *in vivo* molecular and anatomical imaging of the vessel wall. The previously engineered dual-modality IVUS/NIRF imaging catheter system was utilized to assess whether ICG-induced fluorescence can be integrated into IVUS cross-sectional arterial images. Indocyanine green-induced 360-degree fluorescence signals, known to target macrophage-rich inflamed plaque areas [14], were integrated into cross-sectional IVUS images of the vessel wall (Fig. 5). IVUS images were reviewed by a trained technician, blind to the NIRF images. NIRF signal enhancement correlated with sites of increased echogenicity (Fig. 5(a), 5(e)), and intimal thickening (Fig. 5(b), 5(c)) identified by the technician on IVUS imaging.

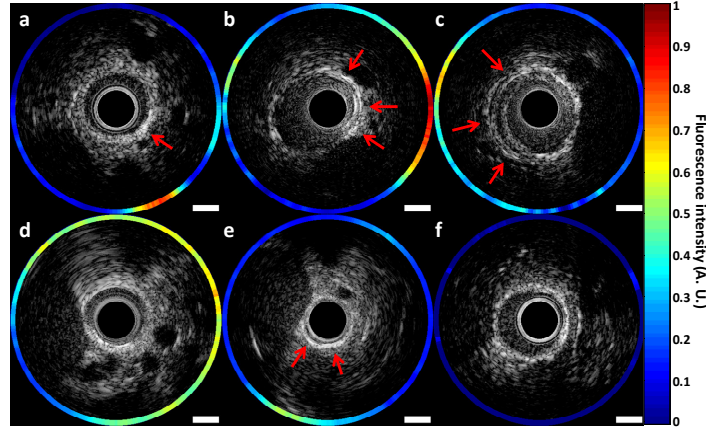


Fig. 5. Integrated intravascular ultrasound (IVUS) and near-infrared fluorescence (NIRF) imaging *in vivo*. (a-e) Integrated IVUS/NIRF images of aortic segments of rabbits fed a cholesterol-enriched diet; (f) image of a rabbit on a regular diet, outside balloon-dilated area. The contour in the IVUS image represents the fluorescence signal intensity. Red arrows show increased echogenicity in (a, e) and intimal thickening in (b, f). Scale bar is 1 mm. A.U., arbitrary units.

Indocyanine green-induced signal enhancement *in vivo* was colocalized with fluorescence *ex vivo* as illustrated in Fig. 6. The cholesterol-enriched diet group that did not undergo balloon injury was excluded from this analysis as in this group, neither macroscopic plaque formation nor significant ICG-accumulation was observed in the abdominal aorta.

We observed that in some arterial segments, *in vivo* ICG-accumulation was stronger as compared to *ex vivo* fluorescence signal intensity while in others it was weaker (Fig. 7(a), 7(c), 7(d), 7(f)). These false positive signals may be due, at least in part, to blood attenuation given an increased distance between the catheter and the vessel wall due to increased vessel dimensions or an eccentric position of the catheter within the artery. Therefore, a compensation algorithm to adjust the fluorescence signal amplitude for blood attenuation was developed, and IVUS images were used to measure the distance between the catheter and the vessel wall at any angle and pullback position. Compensated ICG-induced fluorescence signals are shown in Fig. 7(b), and 7(e), 7(h). False positive fluorescence detection was reduced after applying the blood attenuation compensation algorithm for *in vivo* fluorescence imaging. For the artery segments presented in Fig. 7, a correlation of the fluorescence signal intensity was performed between *in vivo* and *ex vivo* measurements, before and after the blood attenuation compensation, and shows a slightly increased R^2 value (from 0.1 to 0.12) with residuals oscillating around zero following compensation, but not prior. Despite compensation, we observed a remaining variability, potentially explained by catheter eccentricity and depth distribution of the fluorophore in the vessel wall.

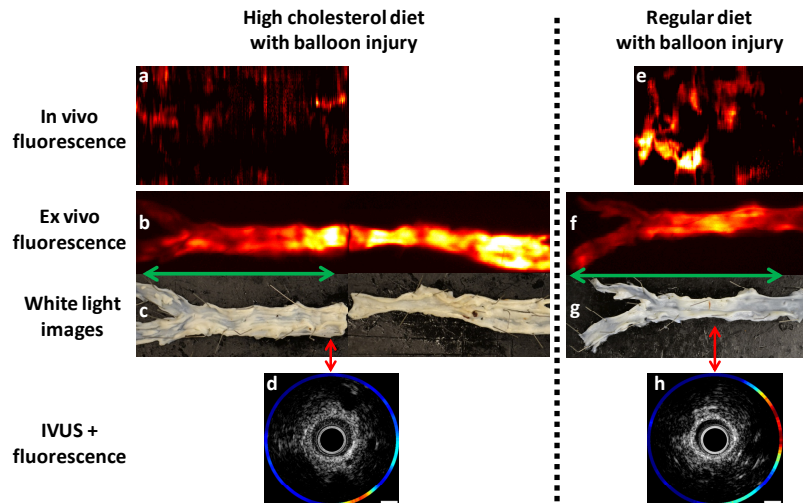


Fig. 6. Comparison of *in vivo* and *ex vivo* near-infrared fluorescence (NIRF) images and corresponding white light images of rabbit aortas. (a, e) *In vivo* fluorescence imaging; (b, f) corresponding *ex vivo* fluorescence imaging; (c, g) white light images of longitudinally opened abdominal aorta and iliac arteries of 2 balloon-injured rabbits. The green arrows show the regions that underwent balloon injury, including the right iliac artery (bottom). The red arrows show corresponding enhanced ICG-accumulation visible in both *in vivo* and *ex vivo* fluorescence imaging. (d, h) Integrated intravascular ultrasound (IVUS)/NIRF cross-sectional images at the locations indicated by the red arrows.

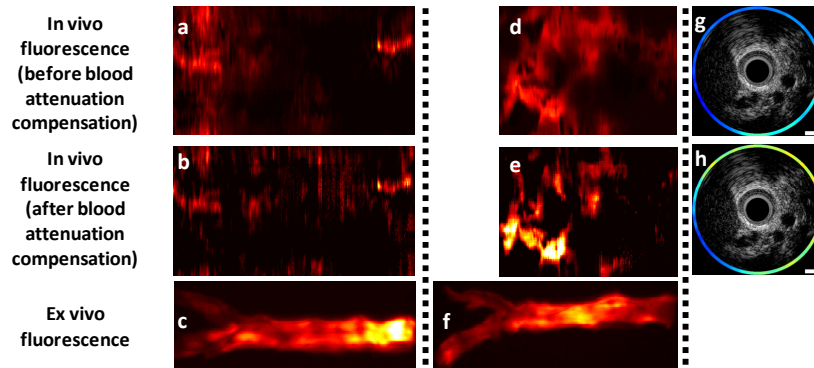


Fig. 7. Effect of blood attenuation compensation on *in vivo* fluorescence images. (a, d, g) *In vivo* fluorescence images of the abdominal aortas of 3 rabbits without blood attenuation compensation; (b, e, h) Corresponding *in vivo* fluorescence images after blood attenuation compensation; (c, f) Corresponding *ex vivo* fluorescence images; (g, h) Integrated intravascular ultrasound (IVUS)/near-infrared fluorescence (NIRF) cross-sectional images (g) without and (h) with blood attenuation compensation.

4. Discussion

This study validates our recently developed bimodal IVUS/NIRF catheter imaging system for *in vivo* plaque imaging in a rabbit model of atherosclerosis. The bimodal intravascular imaging system integrating both ICG-induced fluorescence and ultrasound imaging provided the capability to simultaneously acquire molecular and structural plaque characteristics. Further, a blood attenuation compensation algorithm to normalize the fluorescence signal intensity to the distance between the catheter and the arterial wall as measured by IVUS was introduced to enhance the accuracy of the imaging system. Indocyanine green fluorescence signal intensity *in vivo* was corroborated by corresponding *ex vivo* fluorescence and white light images of macroscopic atherosclerotic plaques.

4.1 Indocyanine green (ICG) and molecular imaging of plaque

Acute coronary syndromes are mainly due to atherosclerotic plaque rupture, thrombus formation, and subsequent vessel occlusion [26]. Emerging molecular imaging strategies aim at identifying inflammatory plaque features, and thereby detecting high-risk plaques prone to rupture, and different molecular agents have been proposed. For over three decades, the fluorochrome ICG has been widely used for different clinical applications including retinal and choroidal vessel imaging or intraoperative evaluation of coronary artery bypass graft patency with proven safety and efficacy [18,27]. Moreover, ICG has previously been demonstrated to target lipid-loaded macrophages *in vitro*, and when utilized as molecular imaging agent to detect lipid-rich, inflamed coronary-sized plaques containing abundant macrophages in atherosclerotic rabbits *in vivo* [14,17,28,29]. Different animal models of atherosclerosis have been established, and are mainly based on pro-atherogenic diets and different types of vessel injury [10,30]. Since rabbit abdominal aorta and iliac arteries suit the typical dimensions of human coronary arteries, rabbit atherosclerosis models are widely used for intravascular imaging studies [31]. Therefore, in this study, different rabbit atherosclerosis models, consisting of cholesterol-enriched diet and/or balloon injury, were utilized to investigate ICG imaging with our bimodal catheter. Balloon injury substantially enhanced ICG accumulation within the vessel wall, and, as expected, the combination of both atherosclerosis inducers was the most effective with this regard. However, ICG accumulation was also correlated with plaques in animals that did not undergo the balloon procedure confirming its potential to image macrophages in this model despite the absence of scar tissue. This is in distinction to previous studies using ICG with balloon-injured aortas [14], as we demonstrated ICG accumulation in a more natural plaque development environment. Moreover, *ex vivo* ICG accumulation, corresponding with *in vivo* fluorescence signals, was colocalized with visible macroscopic inflamed plaque formation on aorta specimen. When integrating *in vivo* fluorescence into cross-sectional IVUS images of the arterial wall, enhanced fluorescence was mainly observed at sites of increased echogenicity, but some regions with lower echogenicity also displayed increased fluorescence. As plaque characterization solely by IVUS imaging is limited, fluorescence imaging adds important information about inflammation features on top of structural plaque characterization.

4.2 Bimodal imaging systems

With traditional fluorescence imaging systems, morphological information about arterial dimensions is lacking. The combination of both fluorescence and IVUS imaging allows for plaque visualization both at the molecular and morphological level, and thereby provides anatomical guidance for fluorescence signal interpretation. With the engineered catheter imaging system, simultaneous image acquisition with high temporo-spatial resolution at frame rates of 10 images/second were achieved [23], while previously reported multimodality imaging systems mainly utilized lower frame rates for fluorescence imaging with larger diameter catheters.

During *in vivo* fluorescence imaging, blood absorption of the fluorescence signal occurs depending on the distance between the catheter and the vessel wall. In the iliac arteries, intense ICG-induced fluorescence signals were observed *in vivo* which were not confirmed *ex vivo*. Separately, in larger arteries and when the imaging catheter was not centered in the vessel, despite substantial ICG accumulation *ex vivo*, only low signal intensity was observed *in vivo* given the increased distance between the catheter and the vessel wall. Hence, molecular and morphological imaging data need to be integrated to allow for an accurate interpretation of *in vivo* measured fluorescence signal intensity. In particular, as the intensity of the fluorescence signal attenuates with increasing distance from the catheter, fluorescence signals need to be adjusted for vessel dimensions. In this study, a blood attenuation compensation algorithm was developed based on measurements of the distance between the

imaging catheter and the vessel wall to adjust fluorescence signals not only for vessel dimensions, but also for eccentric catheter positions. Application of the blood attenuation compensation algorithm reduced false positive, and enhanced true positive fluorescence signals. Similarly, a distance compensation algorithm has previously been proposed for a bimodal OCT/NIRF imaging system [17].

4.3 Limitations

The proposed blood attenuation compensation algorithm based on IVUS co-registration aimed at reducing the above-described inherent technical limitations, but was not able to overcome them completely. With the engineered catheter system and ICG as fluorochrome, fluorescence could not be detected at catheter-vessel wall distance exceeding 1 mm, because the signal was too low. Therefore, plaque analysis in both modalities together could be assessed only where the distance between the catheter and the arterial wall was below 1 mm, and vessels with a diameter between 2 mm and 3 mm were ideal for this experiment. SNR improvements combined to a more robust compensation algorithm could resolve this issue. Saline flushing, potentially combined with partial or full vessel occlusion, might also be considered to increase the sensitivity of the catheter imaging system. In that case, faster pullback speeds should be investigated to limit the injected volume. Also, an over-the-wire approach may favor a centered catheter position. As only modest abdominal aorta and iliac plaque formation was observed in the cholesterol-enriched diet group, a more aggressive diet could have been used to further enhance plaque formation. It would also enable quantifying plaque volumes in IVUS and correlating it with NIRF signal enhancement.

5. Conclusion

The bimodal IVUS/NIRF imaging catheter system, previously engineered by our group, was validated for *in vivo* plaque imaging in a rabbit atherosclerosis model. Simultaneously acquired IVUS/NIRF images of the vessel wall were acquired and allowed for an integrated molecular and structural analysis. Integrating molecular and IVUS imaging in a single catheter, ICG-based fluorescence for *in vivo* molecular imaging was further advanced, and in near future, the identification of lipid-rich, inflamed plaques prone to rupture might become possible. Thereby, high-resolution multimodality imaging technologies may provide new avenues for coronary plaque characterization utilized both in clinical practice and research applications.

Acknowledgments

Maxime Abran was supported by a doctoral scholarship from Natural Sciences and Engineering Research Council of Canada (NSERC). Barbara E. Stähli was supported by the Gottfried-und-Julia-Bangerter-Rhyner Foundation, the Novartis Foundation for Medical-Biological Research (13B067), and the Swiss Foundation for Medical-Biological Scholarships (SSMBS; No P3SMP3_151740/1). This work was funded by a Canadian Institutes of Health Research (Lesage, and Tardif, #273578) and Natural Sciences and Engineering Research Council of Canada (NSERC, 239876-2011) discovery grant to F. Lesage.